The Astrophysical Journal, 965:24 (8pp), 2024 April 10 https://doi.org/10.3847/1538-4357/ad2ea7

Petrogenesis of Erg Chech 002 Achondrite and Implications for an Altered Magma Ocean

Ziliang Jin[1], Yishen Zhang[2,3], Maitrayee Bose[4], Sarah Glynn[5], and Frédéric Couffignal[6]

[1] Macau University of Science and Technology, Taipa, 999078, Macao, People's Republic of China; zljin@must.edu.mo
[2] Department of Earth and Environmental Sciences, KU Leuven, 3000, Leuven, Belgium
[3] Department of Earth, Environmental and Planetary Sciences, Rice University, 6100 Main Street, MS 126, Houston, TX 77005, USA
[4] School of Earth and Space Exploration, Arizona State University, Tempe, AZ 85287-1404, USA
[5] School of Geosciences, University of the Witwatersrand, PVT Bag 3, Wits, Johannesburg 2050, South Africa
[6] GFZ German Research Centre for Geosciences, Telegrafenberg, Potsdam 14473, Germany

Received 2023 November 28; revised 2024 February 21; accepted 2024 February 25; published 2024 April 2

Abstract

This study conducts mineralogical and chemical investigations on the oldest achondrite, Erg Chech 002 (~4565 million yr old). This meteorite exhibits a disequilibrium igneous texture characterized by high-Mg-number (atomic $\mathrm{Mg}/(\mathrm{Mg}+\mathrm{Fe}^{2+})$) orthopyroxene xenocrysts (Mg number = 60–80) embedded in an andesitic groundmass. Our research reveals that these xenocrysts were early formed crystals, loosely accumulated or scattered in the short-period magma ocean on the parent body. Subsequently, these crystals underwent agitation due to the influx of external materials. The assimilation of these materials enriched the ^{16}O component of the magma ocean and induced a relatively reduced state. Furthermore, this process significantly cooled the magma ocean and inhibited the evaporation of alkali elements, leading to elevated concentrations of Na and K within the meteorite. Our findings suggest that the introduced materials are probably sourced from the reservoirs of CR clan meteorites, indicating extensive transport and mixing of materials within the early solar system.

Unified Astronomy Thesaurus concepts: Achondrites (15); Planetesimals (1259); Planetary system evolution (2292)

1. Introduction

Extensive intermediate-felsic magmatism was once thought to be exclusive to Earth until the discovery of several ancient intermediate achondrites over the past decade, including GRA 06128/9 (Day et al. 2009; Shearer et al. 2010), NWA 11119 (Srinivasan et al. 2018), and Erg chech 002 (Barrat et al. 2021). These achondrites typically contain high silica contents (up to 61 percent by weight, wt%), and some are also alkali enriched ($\mathrm{Na_2O} + \mathrm{K_2O} > 4$ wt%; e.g., GRA 06128/9, ALM-A, and Erg chech 002). These samples have not only expanded the diversity of the early solar system rocks and the parent asteroid compositions but also revealed the existence of intermediate-felsic magmatism in early solar system bodies. Currently, the petrogenesis of these high silica achondrites remains an enigma although melting experiments have suggested that low-degree partial melting of ordinary and carbonaceous chondritic materials can generate high Si–Al-alkali melts (Collinet & Grove 2020). Intermediate-felsic magmatism on Earth that contributes to the establishment of a buoyant continental crust requires the development of differentiated mantle through mass circulation on a global scale and the involvement of volatiles, water in particular (Kushiro 1972; Carmichael 2002; Kelemen et al. 2003). However, it is unclear whether the parent bodies of these recently discovered intermediate achondrites have undergone these complex processes.

The recently discovered ungrouped achondrite Erg Chech 002 (EC 002) has been dated as the oldest magmatic achondrite (0.7–2.25 Ma after the formation of calcium–aluminum-rich inclusions, CAIs) and provides evidence for very early volcanism in the nascent solar system (Barrat et al. 2021; Anand et al. 2022; Fang et al. 2022; Zhu et al. 2022; Connelly et al. 2023; Dai et al. 2023; Krestianinov et al. 2023; Reger et al. 2023). The investigations into this meteorite thus benefit our understanding on the driving source for the generation of intermediate-felsic magmatism in the early solar system. Notably, this meteorite exhibits a disequilibrium igneous texture, i.e., coarse-grained high-Mg-number (atomic $\mathrm{Mg}/(\mathrm{Mg}+\mathrm{Fe}) \times 100 = 80$) orthopyroxene (Opx) xenocrysts that supposedly originated from more primitive melts are set in an evolved andesitic groundmass. This peculiar texture could have preserved evidence of multistage magmatic processes experienced by the parent body. For example, the xenocrysts have been considered as either early cumulations crystallized from a primitive magma or residual minerals of the magma source in the parent body (Barrat et al. 2021; Nicklas et al. 2022; Zhu et al. 2022). However, neither of these scenarios adequately explains the formation of the high-alkali andesitic groundmass. Previous studies have revealed notable variations in ϵ^{54}Cr values within EC 002 samples (Anand et al. 2022; Zhu et al. 2022). In addition, the Cr spinels in EC 002 are characterized by variable compositions (Barrat et al. 2021). Thus, discerning the origins of these Cr spinels is crucial for explaining the disparate Cr isotopic signatures and unraveling the processes occurring within the parent body. Moreover, the advancement of ion probe technique allows in situ studying the oxygen isotope behavior in the xenocrysts and groundmass minerals at microscales (<50 μm), thereby providing significant opportunities to evaluate the isotopic alterations in these phases. Accordingly, in this study we reassess the disequilibrium petrographic texture of EC 002 and interpret the magmatic processes in its parent bodies based on the in situ chemical and isotopic analysis of various mineral

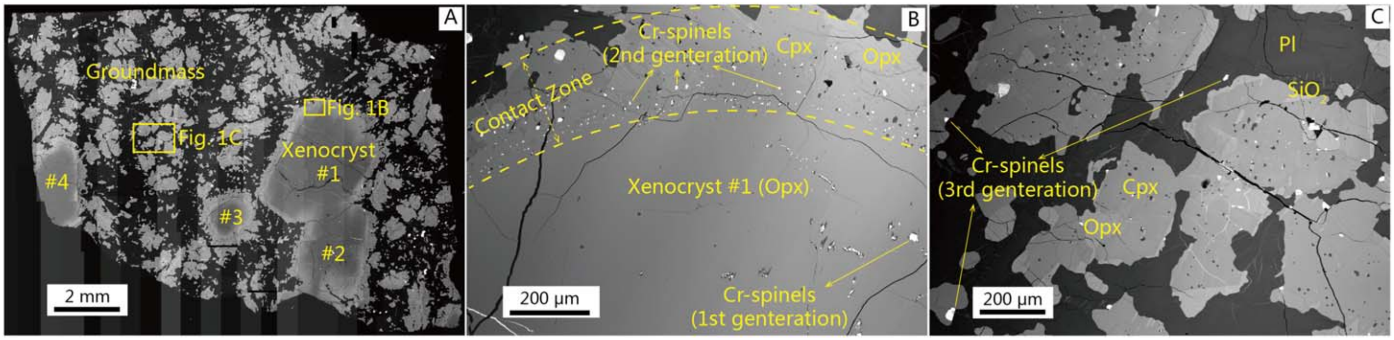

Figure 1. Backscattered electron images of EC 002 sectors. (A) An overview image of the studied EC 002 chip showing four xenocrysts. Two rectangles denote the areas shown in (B) and (C). (B) A close-up of the xenocryst #1, including mineral inclusions such as first-generation Cr spinels and the CZ that features overgrown orthopyroxene (Opx), clinopyroxene (Cpx), and second-generation Cr spinels along the inner boundary. (C) A detailed image of the groundmass that contains Opx, Cpx, plagioclase (Pl), silica (SiO_2), and the third-generation Cr spinels.

phases. Our findings elucidate the amalgamation of materials from diverse sources incorporated into the short-period magma ocean on the parent body of EC 002. This process significantly altered the isotopic signatures and redox status during differentiation, consequently contributing to the formation of the observed disequilibrium igneous texture and the meteorite's high-alkali contents. Moreover, our research suggests that extensive material exchange within the protoplanetary disk transpired within the initial 3 million years, exerting a pivotal influence on the evolutionary trajectory of small bodies.

2. Sample Description and Analytical Results

The EC 002 chip studied here exhibits a similar porphyritic texture (Figure 1) to those of the previously documented samples (Barrat et al. 2021; Nicklas et al. 2022; Zhu et al. 2022). It contains several large euhedral Opx xenocrysts (22% by volume, vol%), a medium-grained groundmass (77 vol%), and pores (<1 vol%). Notably, our sample diverges from the reported one in Barrat et al. (2021) by lacking olivine xenocrysts. The absence of impact-induced destruction to these xenocrysts precludes their external origin. The groundmass consists of lath-shaped plagioclase, anhedral clinopyroxene (Cpx), Opx, spinel, and silica phases (Figure 1(C)). Both Cpx and Opx minerals in the groundmass exhibit extensive lamellae textures. Barrat et al. (2021) have reported that the major compositions of the groundmass phases closely resemble those of andesite. Furthermore, Nicklas et al. (2022) conducted comprehensive measurements of the highly siderophile elements (HSEs) in bulk EC 002, which unveiled a fractionated HSE pattern, indicating the potential core–mantle segregation in the evolutionary history of the parent body. To further constrain the petrogenesis of EC 002, we conduct the analytical experiments of mineral chemistry and in situ oxygen isotopes of pyroxene minerals. Detailed analytical methods and data are given in the Appendix.

2.1. Mineral Chemistry

The chemical compositions of the measured minerals are available as three supplementary Excel tables in Zenodo at doi:10.5281/zenodo.10612541. The tables give the chemical compositions of the pryroxene, Cr spinel, and plagioclase minerals. The compositions of the core area of the Opx xenocrysts resemble those reported previously (Barrat et al. 2021; Nicklas et al. 2022; Zhu et al. 2022) and show a compositional range in the enstatite (En)–ferrosilite (Fs)–wollastonite (Wo) system of $En_{78.6-80.6}Fs_{16.1-17.0}Wo_{2.5-4.7}$ (Figure 2(A)). From the core to the rim, the xenocrysts show a trend of decreasing En components (from En_{80} to En_{60}). Fine-grained minerals hosted in the xenocrysts include Cpx (on average $En_{49.6}Fs_{7.8}Wo_{42.7}$), chromium spinel (Cr spinel), plagioclase (An < 10), and a silica phase.

The average chemical compositions of the Cpx and Opx in the groundmass are $En_{37.7}Fs_{24.9}Wo_{37.4}$ and $En_{46.3}Fs_{48.8}Wo_{4.9}$, respectively. A sharp contact zone (CZ) has been recognized between the xenocrysts and the groundmass (Figure 1(B)). The CZ contains mostly Cpx and a small amount of Opx. On average, both Cpx ($En_{41.3}Fs_{22.5}Wo_{36.2}$) and Opx ($En_{51.7}Fs_{43.3}Wo_{5.1}$) minerals in the CZ contain more En and less Fs content than those in the groundmass (Figure 2(A)).

Cr spinel is usually refractory and is an important indicator of the physicochemical conditions under which its host rocks have formed (Barnes & Roeder 2001). Based on their occurrence and chemistry, we identify three generations of Cr spinels in the sample. The first-generation Cr spinels occur as mineral inclusions hosted in the xenocrysts and are the earliest Cr spinels in the sample (Figure 1(B)). They contain the highest Cr_2O_3 contents of 58.85–63.85 wt%. The second-generation Cr spinels occur along with the overgrown pyroxene minerals around the grain boundaries of the xenocrysts (Figure 1(B)). They formed once the xenocrysts came into contact with the groundmass magma. The third-generation ones are the youngest Cr spinels that present interstitial to the groundmass pyroxene and plagioclase minerals (Figure 1(C)). The average Cr_2O_3 concentration in the second- and third-generation Cr spinels are 50.70 wt% and 42.24 wt% respectively (Figure 2(B)). The average TiO_2 content in the second- and third-generation is 5.37 wt% and 10.16 wt%, much higher than that of the first-generation Cr spinels (0.25 wt%). The Al_2O_3 contents of all three generations are indistinguishable, ranging from 1.34 wt% to 8.98 wt%.

2.2. Trace Elemental Concentrations of Orthopyroxenes

The concentrations of trace elements in 15 xenocryst spots and 7 Opx grains within the groundmass are provided in a fourth supplemental Excel table in Zenodo at doi:10.5281/zenodo.10612541. The trace elemental compositions are in parts per millionby weight of the pyroxene minerals. Rare earth elements (REEs) in the measured spots were normalized against the recommended values for CI chondrites (McDonough & Sun 1995), and their patterns are displayed in Figure 3. The measured xenocrysts exhibit notably low

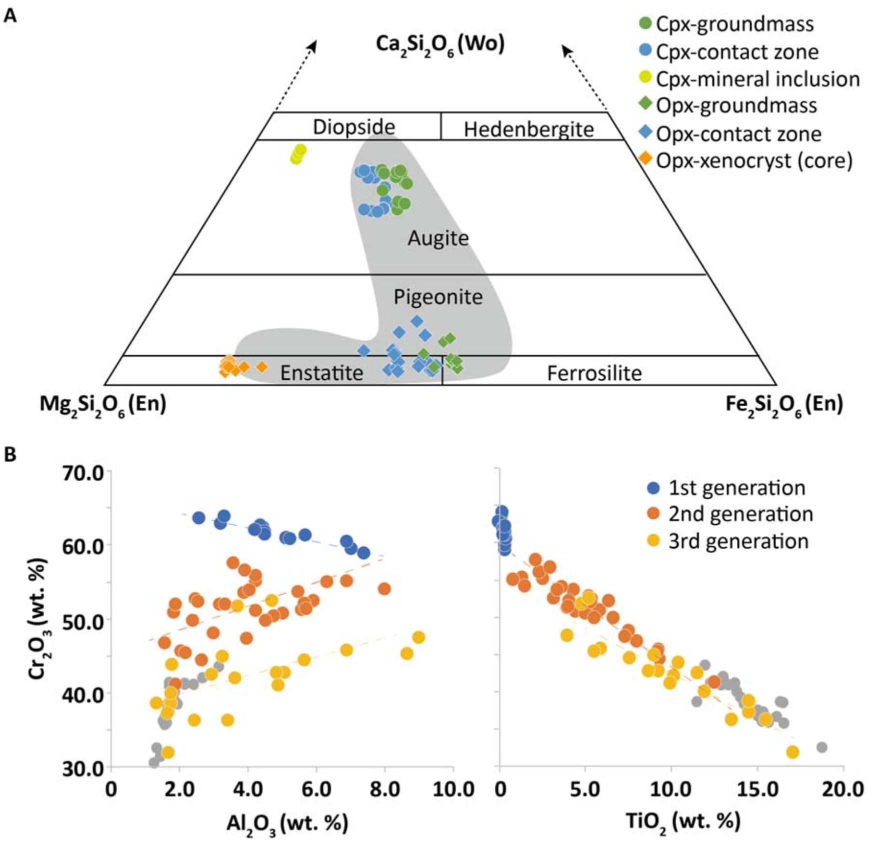

Figure 2. Chemical compositions of pyroxene and Cr-spinel minerals in EC 002. (A) Major element compositions of orthopyroxene (Opx) and clinopyroxene (Cpx) minerals on the pyroxene quadrilateral. The En components of the Opx and Cpx minerals in the CZ are higher than those in the groundmass and lower than the xenocrysts and the Cpx inclusions, indicating the mixing process of melts from two different reservoirs. The gray-shaded area indicates the compositional range of pyroxenes in previously reported samples (Barrat et al. 2021; Nicklas et al. 2022; Zhu et al. 2022). (B) Plots of Cr_2O_3 vs. Al_2O_3 and Cr_2O_3 vs. TiO_2 of three generations of Cr spinels. In both plots, the second- and third-generation Cr spinels show parallel and coincident trend lines, which are distinct from those of the first-generation ones. For comparison, the analytical results of the Cr spinels reported in Nicklas et al. (2022) and Zhu et al. (2022) are plotted as the gray solid circles. The relative error of each point is smaller than the markers.

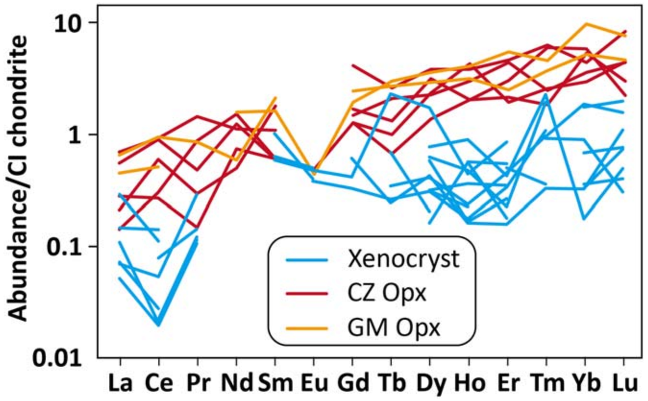

Figure 3. CI chondrite-normalized rare earth element (REE) patterns of xenocrysts and orthopyroxenes (Opx) from the contact zone (CZ) and groundmass (GM). REE contents in CZ and CM Opxs are indistinguishable and higher than those of the xenocrysts. REE concentrations of CI chondrite are from McDonough & Sun (1995).

contents of light REEs, particularly the absence of Nd. Conversely, the heavy REE (Dy, Ho, Er, Tm, Yb, and Lu) contents surpass those of the light REEs and demonstrate a trend parallel to that of CI chondrites. In contrast, the REE contents in the Opx within the groundmass are approximately 1 magnitude higher than those in the xenocrysts. These Opx show an enrichment of heavy REEs.

2.3. In Situ Oxygen Analysis

The $\delta^{18}O$ values of the measured minerals are obtained by normalizing their $^{18}O/^{16}O$ ratios to that of Standard Mean ocean Water ($^{18}O/^{16}O = 0.0020052$; Baertschi 1976) and are listed in a fifth supplementary Excel table in Zenodo at doi:10.5281/zenodo.10612541. The data of two analyzed spots on the cracks were stripped. The xenocrysts show the highest $\delta^{18}O$ value (2.79–3.66‰), which is distinct from that of the pyroxene minerals in the CZ (1.79–2.55‰) and groundmass (2.21–2.89‰). In order to evaluate whether the MgO or FeO components in the pyroxene minerals contributed to the heterogeneity of the results, we plotted the $\delta^{18}O$ value of the measured pyroxene minerals against their En components. As depicted in Figure 4, no evident intragroup and intergroup correlation was observed between the $\delta^{18}O$ and En values, suggesting that the different MgO or FeO contents in pyroxenes had minimal impact on the instrumental mass fractionation and the discrepancies in the $\delta^{18}O$ value among the data sets were the consequences of magmatic processes.

3. Discussion

The origin of the disequilibrium texture observed in EC 002 remains ambiguous. Several previous studies have discussed the disequilibrium texture in EC 002. For example, the chronological study of Zhu et al. (2022) revealed a difference

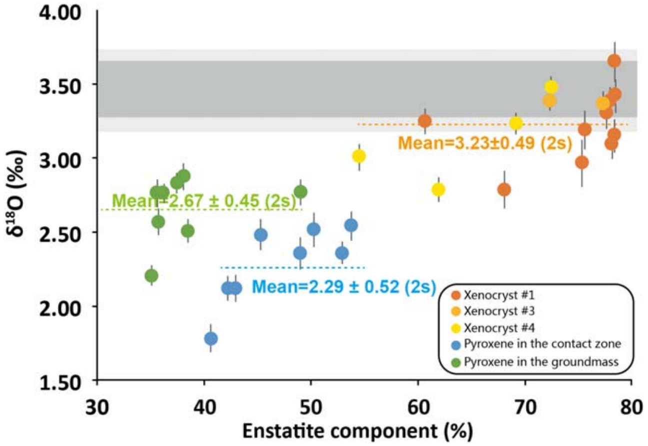

Figure 4. Scatterplot of oxygen isotopic compositions vs. En components of pyroxene minerals in EC 002. The δ^{18}O values of the xenocrysts (#1, #3, and #4) and the pyroxenes from the CZ and groundmass are plotted. The uncertainty for each data point is 0.1‰ (1δ). The gray and light gray bars indicate the ranges of the previously reported δ^{18}O values of the xenocrysts and groundmass, respectively. Both Cpx and Opx minerals have been measured. No significant intergroup correlation between the δ^{18}O values and En components is shown.

in the ages of the old xenocrysts and the young groundmass. In addition, Nicklas et al. (2022) proposed a two-stage formation event such that the xenocrysts represented early mineral cumulations entrapped by subsequent andesitic magma. However, the anticipated texture characteristic of intergrown crystals signifying the presence of mineral cumulations has not been identified in EC 002 (Mercier & Nicolas 1975). Instead, the xenocrysts found in all reported EC 002 fragments exist as sizeable individual grains (>1.5 mm). This observation prompts two potential scenarios: either (1) these crystals originated from a loosely consolidated crystal mush within a deep chamber and were later carried into a shallow magma chamber within a nested magma plumbing system, or (2) they constituted early formed crystals in a small-scale magma ocean, subsequently agitated and dispersed randomly within the parent body. The concept of a plumbing system typically entails the partial melting of the mantle within a differentiated parent body, necessitating significant heat and magma convection in a large-scale magma chamber. However, this seems impractical in a parent body of a size range around ∼20–30 km (Neumann et al. 2023). Furthermore, the low REE content of the xenocrysts dismisses the possibility that they derive from partial melts of a differentiated planetary mantle. Consequently, it is more plausible that these xenocrysts represent minerals that precipitated early within a magma ocean. In the following sessions, we delve into an analysis of how the isotopic and redox characteristics of the short-lived magma ocean underwent alterations, drawing from our analytical results.

3.1. Intragroup and Intergroup Variations of ^{18}O/^{16}O Ratios

As illustrated in Figure 4, pyroxene minerals within different groups exhibit distinct δ^{18}O values, ranging from 1.79‰ to 3.66‰. However, direct comparison of these values is not feasible due to isotopic fractionation effects, such as kinetic fractionation and Rayleigh fractionation. In igneous systems, the fractionation of oxygen isotopes due to crystallization, namely fractional or Rayleigh crystallization, is a prevalent process (e.g., Taylor 1968; Eiler et al. 1996; Zhao & Zheng 2003). This process represents a situation where crystals are instantaneously in equilibrium with the melt they form but are immediately removed from contact with the melt. In contrast, kinetic fractionation of oxygen isotopes typically occurs in short-term events, where timescales are insufficient for isotopes in different reservoirs to reach equilibrium (Herwartz 2021; White 2023). In the EC 002 sample, CZ and groundmass pyroxenes crystallized from a shared magma source without experiencing secondary alteration. Thus, intragroup variations in the ^{18}O/^{16}O ratios of these two types of minerals resulted from crystal fractionation. Potential effects of kinetic fractionation on the oxygen isotopes of the xenocrysts need to be considered as these early minerals exhibit textural disequilibrium with the groundmass phase. Contact with groundmass melts could have led to oxygen isotope diffusion, potentially altering the pristine signature. However, we believe the oxygen isotopic signatures of the xenocrysts remain unaffected by kinetic fractionation. This is because the analyzed points were set in the core areas of the coarse crystals, where no diffusion of elements occurred. For instance, in these regions, constant Mg number values indicate minimal diffusion of Fe and Mg. Given that the diffusion coefficient of oxygen is generally smaller than that of Fe–Mg in En (Farver 2010; Dohmen et al. 2016), oxygen isotope diffusion in the xenocrysts' core areas is improbable. Therefore, the various ^{18}O/^{16}O ratios of the measured minerals stem from the crystal fractionation process and can provide a reasonable estimate of the ^{18}O/^{16}O ratios of the melts where they crystallized.

Moreover, the degree of oxygen isotope fractionation between the mineral and the melts, denoted as $\Delta(\delta^{18}\mathrm{O}_{\mathrm{melts}} - \delta^{18}\mathrm{O}_{\mathrm{minerals}})$, during crystallization closely correlates with temperature (Bindeman et al. 2004). Since the temperature of the melts wherein minerals crystallize fluctuates within a range, the ^{18}O/^{16}O ratios of the measured minerals may display intergroup variations, as observed in our sample.

3.2. Addition of ^{16}O-enriched Material into a Short-period Magma Ocean

In order to evaluate the degree of oxygen isotope fractionation between the mineral and the melts, the temperature of the equilibrated melts to the minerals must be meticulously estimated. Common methodologies for estimating pyroxene crystallization temperature typically rely on both pyroxene and coexisting melt composition (Putirka 2008) as well as pyroxene-only thermometry (e.g., Jorgenson et al. 2022). However, the precision of temperature estimates using these methods heavily relies on calibration data sets, particularly the melt composition (Wieser et al. 2023). The lack of experiments conducted on compositions similar to EC 002 results in an insufficient database to expand previous calibrations that were primarily built on Earth-like compositions. As a result, we employed the newly revised two-pyroxene thermometry based on the calibration by Lindsley & Andersen (1983) and extended with pyroxenes from ordinary chondrites (Nakamuta et al. 2017). The temperatures were calculated using the compositions of Cpx and Opx, represented by the following equations: T (for clinopyroxene) $= 860.9 - 1.548 \times \mathrm{Wo}^2 + 70.55 \times \mathrm{Wo} + 0.3166 \times \mathrm{Fs}^2 - 23.51 \times \mathrm{Fs}$, and T (for Opx) $= 601.9 - 14.60 \times \mathrm{Wo}^2 + 227.3 \times \mathrm{Wo} - 0.1587 \times \mathrm{Fs}^2 - 1.708 \times \mathrm{Fs}$, where Wo and Fs denote the Wo and Fs contents, respectively.

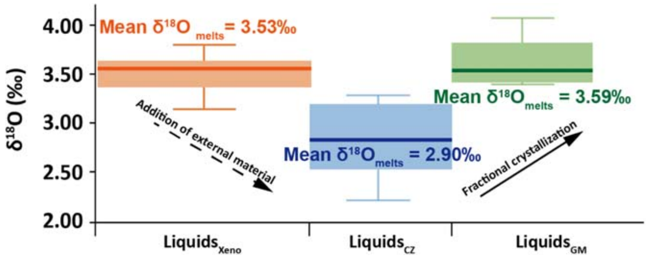

Figure 5. Box plots of oxygen isotopic compositions of melts in equilibrium with measured pyroxene minerals in EC 002. The boxes indicate the interquartile range, covering values between the first and third quartiles of each data set. The upper and lower whiskers represent data points outside the interquartile range. The solid line within each box represents the mean value of a data set. Notably, the δ^{18}O values of Liquids$_{\mathrm{CZ}}$ are lower than those of Liquids$_{\mathrm{Xeno}}$, suggesting the introduction of ^{16}O-enriched materials. Additionally, the elevated δ^{18}O values of Liquids$_{\mathrm{GM}}$ result from the crystallization of pyroxene minerals within the CZ.

Based on these calculations, the estimated crystallization temperatures of the xenocrysts (core area), pyroxenes in CZs, and groundmass are approximately 1133°C–1292°C, 764°C–1216°C, and 858°C–1087°C, respectively. Utilizing these temperature estimates, we computed the δ^{18}O values of the parental melts in equilibrium with the pyroxene minerals using the equation: $\Delta(\delta^{18}\mathrm{O}_{\mathrm{melts}} - \delta^{18}\mathrm{O}_{\mathrm{minerals}}) = -0.0033 \times T$ (°C) + 4.16, where T represents the crystallization temperature of the pyroxene mineral (Bindeman et al. 2004). According to our calculations, the δ^{18}O values of the equilibrated liquids in equilibrium with xenocrysts (Liquids$_{\mathrm{Xeno}}$), pyroxenes in CZs (Liquids$_{\mathrm{CZ}}$), and groundmass (Liquids$_{\mathrm{GM}}$) range from 3.12 to 4.08‰ (mean = 3.53±0.26‰, 1σ), 2.18–4.19‰ (mean = 2.90 ±0.51‰, 1σ), and 3.38–4.06‰ (mean = 3.59±0.24‰, 1σ), respectively (Figure 5). Notably, the δ^{18}O values of Liquids$_{\mathrm{GM}}$ are consistent with previously reported bulk δ^{18}O values of the groundmass component obtained by laser fluorination technique (3.201–3.728‰, Meteoritical Bulletin Database 2020), supporting the rationale of our temperature and δ^{18}O value estimation approaches. Consequently, our data indicate two independent events that led to the enrichments of ^{16}O and subsequently ^{18}O in the short-period magma ocean stage.

Generally, in an evolving magmatic system, the crystallization of mafic minerals, such as olivine and pyroxene, can lead to the enrichment of ^{18}O in the residual melts as these minerals preferentially retain ^{16}O (Matsuhisa et al. 1973; Muehlenbachs & Byerly 1982; Bindeman 2008). In the case of EC 002, the elevated ^{18}O values of the Liquids$_{\mathrm{GM}}$ relative to the Liquids$_{\mathrm{CZ}}$ melts could be attributed to the crystallization of CZ minerals. Conversely, from Liquids$_{\mathrm{Xeno}}$ to the more ^{16}O-enriched Liquids$_{\mathrm{CZ}}$, the most plausible mechanism is the addition of external materials to the magma ocean, leading to its enrichment of ^{16}O.

3.3. Redox Change of the Magma Ocean

Alongside the enrichment of ^{16}O, the differentiation of the parent body underwent a shift toward a more reduced state. Within the three generations of Cr spinels, the second- and third-generation Cr spinels exhibit parallel trends in Cr_2O_3 versus Al_2O_3 and similar trends in Cr_2O_3 versus TiO_2 plots (Figure 2(B)), distinguishing them from the first-generation Cr spinels. These differences signify an alteration during the magmatic differentiation. Notably, the V/(Cr+Al) atomic ratio of Cr spinel acts as a relative indicator of magma redox, as the partitioning coefficient of V significantly decreases with rising oxygen fugacity (Papike et al. 2004). As depicted in Figure 6, Cr spinels within the CZ and groundmass (second and third generations) display indistinguishable V/(Cr+Al) values, which are higher than those observed in the Cr spinels (1st generation) found in the Opx xenocryst. This observation suggests that the magmas contributing to the formation of the groundmass and CZ (Liquids$_{\mathrm{CZ}}$ and Liquids$_{\mathrm{GM}}$) were more reduced in comparison to the melts where the xenocrysts crystallized (Liquids$_{\mathrm{Xeno}}$).

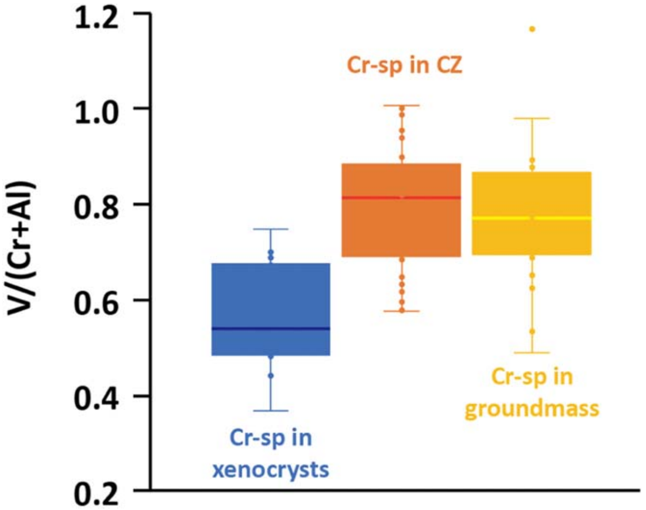

Figure 6. Box plots of V/(Cr+Al) values for all generations of Cr spinels. The interquartile ranges of the V/(Cr+Al) values for the second and third generations, which formed in the CZ and groundmass, are indistinguishable and higher than those of the first-generation Cr spinels hosted in the xenocrysts as melt inclusions.

3.4. Retention of Alkalis in the Magma Ocean

The introduction of mixed materials likely accounts for the elevated alkali contents in the groundmass. During the magma ocean stage of differentiated planetesimals, the loss of moderately volatile elements (MVEs) through degassing can lead to the depletion of these elements. Thus, the high concentrations of alkali elements in EC 002 present an enigma. Collinet & Grove (2020) attempted to reproduce the alkali-undepleted signature of some (trachy)andesite achondrites through closed-system melting experiments (temperature = 1063°C–1300°C and pressure = 2–13 MPa). Their results demonstrated that low-degree partial melting of (a) chondrite parent bodies could generate Si–Al-alkali-rich melts. Note that special molybdenum hafnium carbide pressure vessels were used in these experiments to prevent the loss of MVEs during melting. However, in an open magmatic system within space environment, this mechanism is not realistic for retaining the MVEs. Alternatively, the addition of external materials during differentiation of the EC 002 parent body offers new insights into the limited loss of alkali elements in an open system. The incorporated materials could substantially decrease the temperature of the magma ocean. Our data reveal that the crystallization temperatures of groundmass pyroxenes were up to 200°C lower than those of the xenocrysts. Since only CZ pyroxene and Cr spinel crystallized during this cooling phase, the significant temperature difference indicates a passive cooling process resulting from the added external materials. Consequently, the evaporation of Na and K during the passive cooling would be notably suppressed at lowered temperatures.

3.5. Potential Sources of the Added Materials

Considering the decreased δ^{18}O values and altered redox condition, we anticipate that the incorporated materials contain a significant amount of materials resembling CR clan meteorites (CB, CH, and CR). Our calculations suggest that the δ^{18}O values of the added materials should fall below 2.18‰ (the lower limit of the δ^{18}O of the Liquids$_{\rm CZ}$). Among the meteorite collections we have, only certain carbonaceous chondrites (CCs), such as CO, CV, CK, CB, CH, and CR types, exhibit δ^{18}O values lower than 2‰ (Greenwood et al. 2020). In addition, within these CCs, pristine CR clan (CB, CH, and CR) meteorites are the most reduced types due to their high metal content. The introduction of these materials can effectively drive the differentiation toward a more reduced state. Moreover, these added materials could have elevated the ϵ^{54}Cr values of the groundmass of EC 002, given the positive ϵ^{54}Cr values observed in materials from the CC reservoir (Trinquier et al. 2007). However, the three generations of the Cr spinels, one of the major containers of Cr, are fine grained, with some even occurring at submicrosizes in EC 002. The challenges in effectively sorting out these fine-grained Cr spinels in EC 002 could have introduced significant uncertainties in determining the Cr isotopic ratios. This is reflected in the heterogeneous ϵ^{54}Cr values observed in bulk EC 002, ranging from −0.35 to −0.73 (Anand et al. 2022; Zhu et al. 2022).

3.6. Evolutional Path of EC 002 Parent Body and Implications

Combining our results with previous studies, we outline the evolutionary history of the parent body of EC 002 in four stages (Figure 7). The first stage (Figure 7(A)) signifies the core–mantle differentiation of the parent body, initiated by the heat released from the decay of short-lived radiogenic elements. This process led to the migration of HSEs into the core, resulting in the observed fractionated pattern in bulk EC 002 (Nicklas et al. 2022). The second stage involved the early crystallization of Opx during a relatively oxidized magma ocean stage (Figure 7(B)). Subsequently, a blend of materials from both inner and outer solar system sources infiltrated the short-period magma ocean. This action churned up the preexisting Opx minerals, reducing the temperature and oxygen fugacity and decreasing the ^{16}O/^{18}O ratio of the magma ocean (Figure 7(C)). The final stage marked the solidification of the altered magma ocean, giving rise to the observed disequilibrium mineral texture (Figure 7(D)).

As Zhu et al. (2022) proposed that EC 002 derived from a brachinite-like body from the inner solar system, the incorporation of CR clan–like materials from the outer solar system materials during differentiation of the EC 002 parent body emphasizes the extensive transfer and exchange of materials between CC and non-CC reservoirs within the solar system. Various hypotheses have been proposed to explain the inward and outward migration of materials in the early solar system (Ciesla 2007; Walsh et al. 2011). These hypotheses suggest that the hybrid accretion of planetesimals was likely a common occurrence in the early stages of the solar disk. On the other hand, the separation of two distinct planetesimal populations, i.e., CC and non-CC reservoirs, was completed within 3 million yr after CAIs (Kruijer et al. 2017; Lichtenberg et al. 2021). Subsequently, the mixing of materials between the two reservoirs was limited and declined over time due to the progressive accretion of the planets. The hybrid accretion of EC 002 parent body within 2 Ma after the CAIs thus indicate that the separation of CC and non-CC reservoirs was coupled with the exchange of materials within the first 3 million yr of the solar system's formation.

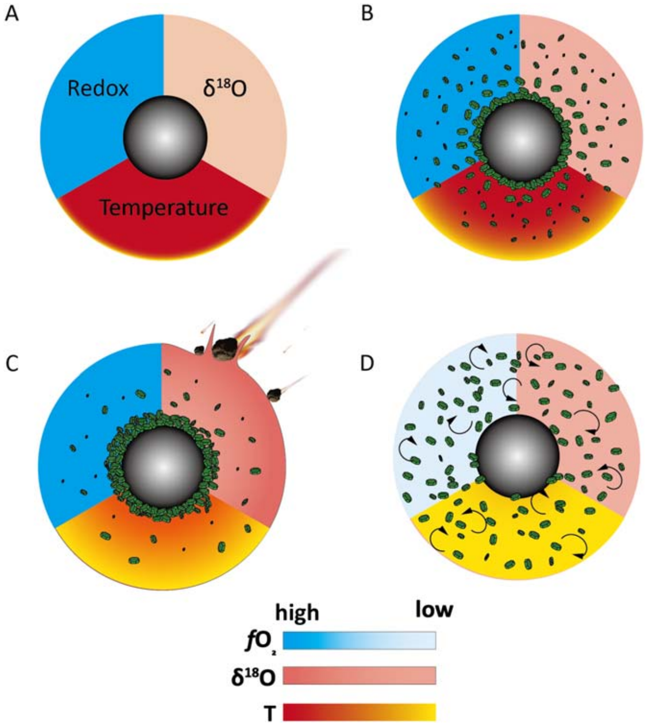

Figure 7. A schematic showing the evolutional history of EC 002 parent body. The whole process is divided into four stages. (A) Initial differentiation of the parent body led to core–mantle segregation and the establishment of a hot and oxidized magma ocean. (B) During the second stage, high-Mg Opx crystallized and loosely accumulated or scattered within the magma ocean. (C) The addition of external materials not only induced cooling and chemical or isotopic alterations in the magma ocean but also disturbed the early formed high-Mg Opx. (D) Eventually, the evenly distributed high-Mg Opx occurs as xenocrysts after the solidification of the parent body.

4. Conclusions

In conclusion, our investigation into the mineral chemistry and oxygen isotopes of the achondrite EC 002 sheds light on the dynamic evolution of its parent body's magma ocean stage, influenced by the introduction of external materials. These incorporated materials likely had a threefold effect on the differentiating asteroid parent body: (1) they decreased the ^{18}O/^{16}O ratio, (2) contributed to the cooling, and (3) induced a reduction in the oxygen fugacity. Combining our findings with previous research, it becomes apparent that the added materials probably comprise substances sourced from the reservoirs of CR clans. This emphasizes the extensive material exchange that transpired within the early solar system and offers new insights into the genesis of intermediate-felsic achondrites.

Acknowledgments

We would like to thank the anonymous reviewer for the constructive comments that significantly improved this manuscript. We are grateful to Dr. Michael Wiedenbeck at GFZ for coordinating and arranging the ion probe analysis sessions. We thank Jingyou Chen and Lei Jin for assistance with the SEM, EDS, and WDS measurements. Z.J. was funded by the Science and Technology Development Fund, Macau SAR (0067/2021/

A and 0018/2022/ITP) and National Natural Science Foundation of China (42203046). The results reported herein benefited from collaborations and/or information exchange within NASA's Nexus for Exoplanet System Science (NExSS) research coordination network sponsored by NASA's Science Mission Directorate and project "Alien Earths" funded under Agreement No. 80NSSC21K0593.

Appendix
Analytical Methods

A.1. Scanning Electron Microscopy

We cut and polished our EC 002 fragment and mounted it in a 1 inch epoxy disk. Scanning electron (SE) and backscattered electron images were obtained by an SE microscope (JEOL JSM IT500) in the State Key Laboratory of Lunar and Planetary Science (SKLplanets) at Macau University of Science and Technology. The equipped Oxford ULTIM Max energy dispersive spectrometer (EDS) was employed to identify the minerals phases.

A.2. Wavelength-dispersive X-Ray Spectroscopy

Concentrations of the major elements of pyroxene, plagioclase, spinel, and silica phases were analyzed by the JXA-iSP100 Electron Probe Microanalyzer in Nanjing Hongchuang Exploration Technology Service Co., Ltd. Analytical conditions were 15 keV acceleration voltage. The beam currents were 10 nA for plagioclase measurements and 20 nA for Cr spinel and pyroxene measurements. The counting times for both the peaks and backgrounds are 50 s for each element. Well-characterized, natural, and synthetic standards (jadeite for Si and Al, titanium for Ti, vanidium for V, orthoclase for K, anhydrite for Ca, albite for Na, magnesium oxide for Mg, chromium oxide for Cr, almandine for Fe, rhodonite for Mn, apatite for P, nickel for Ni) were used for calibration and to confirm the analytical precision (within 98% accuracy). Detection limits were 0.03 wt% for K_2O, CaO, Al_2O_3, SiO_2, Na_2O, and MgO; 0.04 wt% for NiO, MnO and Cr_2O_3; 0.05 wt% for V_2O_3; and 0.06 wt% for FeO.

A.3. Laser Ablation Inductively Coupled Plasma Mass Spectrometry

The compositions of trace elements in both the xenocrysts and Opx minerals within the groundmass were analyzed using the Laser Ablation Inductively Coupled Plasma Mass Spectrometry system in the SKLplanets. The selected mineral grains were ablated by the GeoLas HD laser system, employing a 32 μm diameter laser beam. The parameters for the laser beam were configured with a pulse frequency of 2 Hz and energy set at 4 mJ cm^{-2}. Ion signals were meticulously captured using the Agilent 7900 Mass Spectrometer. During the analytical process, He gas functioned as the carrier gas, while Ar served as the nebulizer gas. Each individual data collection point necessitated ~90 s, comprising 45 s for background sampling and 45 s for effective signal collection. For internal standardization, ^{29}Si was employed. To ensure accuracy and precision in the analytical procedure and subsequent data reduction, Standard Reference Materials 610 and 612 (SRM 610 and 612) were employed. The data calibration was performed using the ICPMSDatacal software (version 10.9, Liu et al. 2008).

A.4. Secondary Ion Mass Spectrometry

We used the Cameca 1280-HR instrument at the Helmholtz Zentrum Potsdam to conduct oxygen isotope determinations on the xenocryst and pyroxene minerals in the CZ and groundmass. Prior to the measurements, the sample was imaged to assist with navigation and point selection using a motorized Nikon Eclipse LVDIA-N microscope. Images of the samples were both taken uncoated and then again after sputter coating with a 35 nm, high-purity gold film. The actual Secondary Ion Mass Spectrometry analyses were made using a 1.8 nA, $^{133}Cs^+$ primary ion beam. Negative secondary ions were extracted using a −10 kV potential on the sample holder and charge compensation involved normal-incidence, low-energy electron flooding. Each analysis was preceded by a 70 s presputtering of the target domain with a 20 μm raster, which both removed the gold coating and established stable sputtering conditions. After completing presputtering, automatic centering routines were applied to the secondary beam in both the *X*- and *Y*-directions on the field aperture, as well as in the *X*-direction for the entrance slits. The instrument was operated in multicollection mode at a mass resolving power of $M/\Delta M \approx 7000$ (at 10% peak height), which was enough to separate ^{18}O (H1) and ^{16}O (L'2). A single analysis of 30 cycles, complete with presputtering and automatic centering routines, lasted approximately 4 minutes. The average pressure in the sample chamber was 4.5×10^{-6} pascals, and data were filtered at the 3σ level. The sample mount was periodically exchanged with a separate mount containing the pyroxene reference materials (RMs): O6JY29 (Cpx), O6JY31 (Cpx), O6JY06 (Opx), and O6JY31 (Opx), which were developed as geochemical RMs for oxygen isotope ratio determinations with $\delta^{18}O_{V-SMOW}$ values of 5.45‰, 5.19‰, 5.75‰, and 5.54‰, respectively (Tang et al. 2019). NIST 610 was used to monitor the drifting of the measurements. Before and after six sample points, two points were measured for NIST 610 and the RMs. In total, the RMs were each measured 19 times in three sessions. The repeatability of the results of RMs in each session are listed here: 0.22‰ 0.29‰, and 0.16‰ for O6JY29; 0.25‰, 0.19‰, and 0.27‰ for O6JY31; 0.25‰, 0.22‰, and 0.16‰ for O6JY06; and 0.08‰, 0.19‰, and 0.33‰ for O6JY31. The true $\delta^{18}O_{V-SMOW}$ values of the RMs were used to determine the mean instrumental mass fractionation (IMF): 1.0005 for Cpx and 0.997 for Opx. These IMF values were then used to correct the measured $^{18}O/^{16}O$ ratio from which the delta value for the unknowns is calculated.

ORCID iDs

Ziliang Jin https://orcid.org/0000-0002-1852-9362
Yishen Zhang https://orcid.org/0000-0002-4261-7565
Maitrayee Bose https://orcid.org/0000-0002-7978-6370
Sarah Glynn https://orcid.org/0000-0002-4584-8422

References

Anand, A., Kruttasch, P. M., & Mezger, K. 2022, M&PS, 57, 2003
Baertschi, P. 1976, E&PSL, 31, 341
Barnes, S. J., & Roeder, P. L. 2001, JPet, 42, 2279
Barrat, J.-A., Chaussidon, M., Yamaguchi, A., et al. 2021, PNAS, 118, e2026129118
Bindeman, I. 2008, RvMG, 69, 445
Bindeman, I. N., Ponomareva, V. V., Bailey, J. C., & Valley, J. W. 2004, GeCoA, 68, 841
Carmichael, I. S. 2002, CoMP, 143, 641

Ciesla, F. J. 2007, Sci, 318, 613
Collinet, M., & Grove, T. L. 2020, GeCoA, 277, 334
Connelly, J., Bollard, J., Amsellem, E., et al. 2023, ApJL, 952, L33
Dai, W., Moynier, F., Fang, L., & Siebert, J. 2023, GChPL, 24, 33
Day, J. M., Ash, R. D., Liu, Y., et al. 2009, Natur, 457, 179
Dohmen, R., Ter Heege, J. H., Becker, H.-W., & Chakraborty, S. 2016, AmMin, 101, 2210
Eiler, J. M., Farley, K. A., Valley, J. W., Hofmann, A. W., & Stolper, E. M. 1996, E&PSL, 144, 453
Fang, L., Frossard, P., Boyet, M., et al. 2022, PNAS, 119, e2120933119
Farver, J. R. 2010, RvMG, 72, 447
Greenwood, R. C., Burbine, T. H., & Franchi, I. A. 2020, GeCoA, 277, 377
Herwartz, D. 2021, RvMG, 86, 291
Jorgenson, C., Higgins, O., Petrelli, M., Bégué, F., & Caricchi, L. 2022, JGRB, 127, e2021JB022904
Kelemen, P. B., Hanghøj, K., & Greene, A. R. 2003, TrGeo, 3, 659
Krestianinov, E., Amelin, Y., Yin, Q.-Z., et al. 2023, NatCo, 14, 4940
Kruijer, T. S., Burkhardt, C., Budde, G., & Kleine, T. 2017, PNAS, 114, 6712
Kushiro, I. 1972, JPet, 13, 311
Lichtenberg, T., Drążkowska, J., Schönbächler, M., Golabek, G. J., & Hands, T. O. 2021, Sci, 371, 365
Lindsley, D. H., & Andersen, D. J. 1983, LPSC, 88, A887
Liu, Y., Hu, Z., Gao, S., et al. 2008, ChGeo, 257, 34
Matsuhisa, Y., Matsubaya, O., & Sakai, H. 1973, CoMP, 39, 277
McDonough, W. F., & Sun, S. S. 1995, ChGeo, 120, 223
Mercier, J. C., & Nicolas, A. 1975, JPet, 16, 454
Meteoritical Bulletin Database 2020, https://www.lpi.usra.edu/meteor/metbull.php?sea=Erg+Chech+002&sfor=names&ants=&nwas=&falls=&valids=&stype=contains&lrec=50&map=ge&browse=&country=All&srt=name&categ=All&mblist=All&rect=&phot=&strewn=&snew=0&pnt=Normal%20table&code=72475
Muehlenbachs, K., & Byerly, G. 1982, CoMP, 79, 76
Nakamuta, Y., Urata, K., Shibata, Y., & Kuwahara, Y. 2017, M&PS, 52, 511
Neumann, W., Luther, R., Trieloff, M., Reger, P. M., & Bouvier, A. 2023, PSJ, 4, 196
Nicklas, R. W., Day, J. M., Gardner-Vandy, K. G., & Udry, A. 2022, NatGe, 15, 696
Papike, J., Karner, J., & Shearer, C. 2004, AmMin, 89, 1557
Putirka, K. D. 2008, RvMG, 69, 61
Reger, P. M., Roebbert, Y., Neumann, W., et al. 2023, GeCoA, 343, 33
Shearer, C. K., Burger, P. V., Neal, C., et al. 2010, GeCoA, 74, 1172
Srinivasan, P., Dunlap, D. R., Agee, C. B., et al. 2018, NatCo, 9, 3036
Tang, G.-Q., Su, B.-X., Li, Q.-L., et al. 2019, GGRes, 43, 585
Taylor, H. P. 1968, CoMP, 19, 1
Trinquier, A., Birck, J.-L., & Allegre, C. J. 2007, ApJ, 655, 1179
Walsh, K. J., Morbidelli, A., Raymond, S. N., O'Brien, D. P., & Mandell, A. M. 2011, Natur, 475, 206
White, W. M. 2023, Isotope Geochemistry (2nd ed.; New York: John Wiley & Sons)
Wieser, P. E., Kent, A. J., Till, C. B., et al. 2023, JPet, 64, egac126
Zhao, Z.-F., & Zheng, Y.-F. 2003, ChGeo, 193, 59
Zhu, K., Becker, H., Li, S.-J., et al. 2022, MNRAS: Letters, 515, L39